The Astrophysical Journal Letters, 878:L7 (8pp), 2019 June 10 https://doi.org/10.3847/2041-8213/ab1f80

Formation of Transition Alumina Dust around Asymptotic Giant Branch Stars: Condensation Experiments using Induction Thermal Plasma Systems

Aki Takigawa[1,2], Tae-Hee Kim[3], Yohei Igami[4], Tatsuki Umemoto[2], Akira Tsuchiyama[2,7], Chiyoe Koike[5], Junya Matsuno[2], and Takayuki Watanabe[6]
[1] The Hakubi Center for Advanced Research, Kyoto University, Kitashirakawa-Oiwakecho, Sakyo, Kyoto 606-8502, Japan; takigawa@kueps.kyoto-u.ac.jp
[2] Division of Earth and Planetary Sciences, Kyoto University, Kitashirakawa-Oiwakecho, Sakyo, Kyoto 606-8502, Japan
[3] Institute for Nuclear Science and Technology, Department of Nuclear and Energy Engineering, Jeju National University, 102 Jejudaehak-ro, Jeju-si, Jeju, 63243, Republic of Korea
[4] Institute of Materials and Systems for Sustainability, Nagoya University, Furo-cho, Chikusa-ku, Nagoya 464-8603, Japan
[5] Department of Physics, Ritsumeikan University, 1-1-1 Nojihigashi, Kusatsu-shi, Shiga 525-8577, Japan
[6] Department of Chemical Engineering, Kyushu University, Fukuoka 819-0395, Japan
Received 2019 February 22; revised 2019 April 21; accepted 2019 May 6; published 2019 June 6

Abstract

Mid-infrared spectroscopic observations of oxygen-rich asymptotic giant branch (AGB) stars show the common presence of dust species that have a broad feature at ∼11–12 μm. Chemically synthesized amorphous alumina (Al_2O_3) is widely accepted as the source of this emission, although it is not obvious that amorphous alumina can condense in circumstellar conditions. We performed condensation experiments of Al–Si–Mg–O and Mg–Al–O gases using induction thermal plasma systems, in which small particles condense from vapors with a steep temperature gradient. The condensates were analyzed using X-ray diffraction and Fourier transform infrared spectroscopy, and observed with a transmission electron microscope. The condensed nanoparticles from the Al and O gases were transition aluminas based on face-centered cubic (fcc) packed oxygen (δ- and λ-alumina, and an unknown phase). The fcc oxygen frameworks were maintained in the condensed alumina containing small amounts of Mg and Si. Condensates from the gases of Al:Mg = 99:1 and 95:5 had δ- and γ-alumina structures. Particles with λ- and γ-alumina structures formed from starting materials of Al:Si = 9:1 and Al:Si:Mg = 8:1:1, respectively. Amorphous silica-rich particles condensed from gases of Al/(Si+Al) < 0.75. The condensed transition alumina containing ∼10% Si showed similar spectral shapes to the observed dust emission from the alumina-rich AGB star T Cep. Based on the present results, it is reasonable that the source of 11–12 μm broad emission of alumina-rich stars is not amorphous alumina, but is transition alumina containing ∼10% Si.

Key words: circumstellar matter – methods: laboratory: solid state – stars: AGB and post-AGB – stars: winds, outflows

1. Introduction

Mid-infrared (MIR) dust emission from oxygen-rich asymptotic giant branch (AGB) stars are classified into several types based on fluxes at 10, 11, and 12 μm (Sloan et al. 2003). About half of the known O-rich AGB stars show clear amorphous silicate emissions at 10 and 18 μm (i.e., they are silicate-rich stars). Dust emission with a broad peak at 11–12 μm is observed for about 40% of O-rich AGB stars. This dust emission cannot be explained by amorphous silicates, but is reproduced by amorphous Al_2O_3 (i.e., they are alumina-rich or aluminum oxide-rich stars). The distribution of gaseous SiO and AlO molecules around the alumina-rich AGB star W Hya shows that >70% of SiO molecules remain gaseous, and the AlO gas distribution matches the dust distribution observed by optical polarimetric imaging (Ohnaka et al. 2016, 2017; Takigawa et al. 2017). These observations indicate the efficient formation of alumina dust around alumina-rich stars. Presolar grains identified in primitive meteorites and cometary dust are survivals of the circumstellar dust of evolved stars that formed prior to the birth of the solar system. Although hundreds of presolar alumina grains have been reported, analysis of the crystal structures were performed for only several of them; this showed that most of the presolar alumina grains analyzed were corundum except for one amorphous alumina grain (Choi 1998; Stroud et al. 2004; Takigawa et al. 2014, 2018).

Amorphous alumina synthesized by sol-gel processing is able to reproduce the broad peak at 11–12 μm, and thus is widely used to fit the dust emission of alumina-rich stars (Begemann et al. 1997). However, such a wet chemical technique (hydrolyzation and polymerization of metal alkoxides) is different to the possible dust-formation processes occurring around stars. The structure of amorphous alumina is not unique because it depends on its density (Gutiérrez & Johansson 2002). In laboratories, amorphous alumina has been prepared not only by sol-gel processing but by the sputter deposition technique, chemical vapor deposition, anodization, and via the oxidation of Al (e.g., Chou & Nieh 1991; Maruyama & Arai 1992; Yakovleva et al. 2000; Trunov et al. 2005).

It is, however, not obvious that amorphous alumina condenses in circumstellar environments. Crystalline aluminas are divided into two types: Al_2O_3 based on hexagonal close packed (hcp) and face-centered cubic (fcc) packed oxygen. There are more than eight transition aluminas, which are metastable alumina phases with different crystal structures,

[7] Present addresses: Research Organization of Science and Technology, Ritsumeikan University, 1-1-1 Nojihigashi, Kusatsu, Shiga 525-8577, Japan, and Guangzhou Institute of Geochemistry, Chinese Academy of Sciences 511 Kehua Street, Wushan, Tianhe District, Guangzhou, 510640, China.

other than the stable phase of Al_2O_3, corundum (α-alumina). Corundum, κ, and χ alumina have hcp oxygen frameworks, whereas γ, η, θ, θ', θ'', δ, and λ aluminas have fcc-packed oxygen. Even from gases undergoing very high cooling, transition (rather than amorphous) alumina might condense, as seen in previous condensation experiments (Tavakoli et al. 2013; Ishizuka et al. 2016). Moreover, amorphous or metastable alumina that forms under strong disequilibrium might contain other elements in their structures, such as Mg and Si, because of the low elemental abundance of Al (Al/Si ~0.08; Lodders 2003).

An induction thermal plasma (ITP) system provides an ultra-high temperature plasma to vaporize refractory materials and a high cooling rate for gases with a sharp temperature gradient where nanoparticles condense. Nanoparticles of silicates with various compositions and textures have been synthesized using ITP systems to study the formation of cometary silicates (Matsuno et al. 2014; Kim et al. 2017). In this study, we perform condensation experiments of gases in the Al–Si–Mg–O system using ITP furnaces. The crystal structures of the condensed particles are examined with X-ray powder diffraction (XRD) and a field-emission transmission electron microscope (FE-TEM). Their MIR spectra are then measured and compared with the dust emission of the alumina-rich star T Cephei.

2. Experiments

2.1. Condensation Experiments

An ITP system consists of a plasma torch, a chamber, and a radio-frequency power supply (Cheng et al. 2012; Kim et al. 2017). Experiments were performed in lower (6 kW) and higher (30 kW) power ITP systems. The experimental conditions are summarized in Table 1.

The condensation experiments that used Al–Si–O gases were performed in the lower-power ITP system (ITP-L; JEOL TP-40020NPS, TP-99010FDR) at Kyoto University, Japan. A mixture of Ar and O_2 was used as the central plasma-forming gas. A plasma jet was generated at a plate power of 6 kW and an induction frequency of 13.6 MHz. Mixtures of metallic Al and Si powders (Koujundo Chemical Lab. Co., Ltd.) were used as starting materials of the experiments in the system of Al–Si–O. The atomic fractions of Al in the starting materials (f_{Al} = [Al]/([Al]+[Si])) were 0, 0.07, 0.5, 0.75, 0.9, and 1.0 (Runs Si_{100}, Al_7Si_{93}, $Al_{75}Si_{25}$, $Al_{90}Si_{10}$, and Al_{100}, respectively). In Run $Al_{80}Si_{10}Mg_{10}$, a crystalline MgO (periclase) powder was used as the starting material in addition to the metallic Al and Si powders, where the atomic ratio of Al:Si:Mg was set at 8:1:1. The higher-power ITP system (ITP-H; JEOL JHS-35M, TP12010) was used for the experiments of Al–Mg–O gases at the Tokyo Institute of Technology, Japan. A plate power and an induction frequency of ITP-H are 30 kW and 4 MHz, respectively. Mixtures of metallic Al and periclase powders with f_{Al} = [Al]/([Al]+[Mg]) of 1, 0.99, and 0.95 (Runs Al_{100}-H, $Al_{99}Mg_1$-H, and $Al_{95}Mg_5$-H, respectively) were used as starting materials. Ar gas at 5 L minute^{-1} was used as a central gas and a mixture of Ar and O_2 gases at 55 and 10 L minute^{-1}, respectively, was used as a sheath gas. We note that the experiments of only Al and O (f_{Al} = 1) were performed in both the low-power (ITP-L) and high-power (ITP-H) ITP systems (Al_{100} and Al_{100}-H) to assess differences between them.

Starting materials are injected into a discharged plasma flame with a carrier gas of Ar and are vaporized at high temperatures (~10,000 K). They react with a discharged oxygen gas to form Al and Si oxides. Steep temperature gradients in the plasma flames provide high cooling rates for the gases (10^4–10^5 K s^{-1}) where nanoparticles subsequently condense. Condensed fine powders were collected at the upper and bottom walls of the reaction chamber in the ITP-L system, and on the wall and filter of the reaction chamber and sample collection filter in the ITP-H system.

2.2. Sample Analysis

The condensed particles were analyzed with XRD (Rigaku SmartLab) using Ni-filtered Cu$K\alpha$ (λ = 1.5418 Å) radiation at an accelerating voltage of 40 kV and a tube current of 40 mA. Silicon zero diffraction plates were used as sample holders. The scan range was 4°–95° 2θ and the scan step interval was 0.02 deg/step. For Fourier transform infrared (FT-IR) spectroscopy, particles were dispersed in a KBr matrix with a mass ratio of 1:200. KBr disks of 5 mm diameter were prepared for all samples. A large pellet of 10 mm diameter with a column density of particles of 0.95 mg cm^{-2} was prepared to determine the reflective index of the condensed particles in Run $Al_{90}Si_{10}$. Transmission spectra of the pellets in the wavenumber range 400–7500 cm^{-1} (1.3–25.0 μm) were measured with JASCO MFT-680 and Thermo Nicolet iS5. Because the XRD and FT-IR spectra showed no differences between samples collected at the upper and bottom walls of the ITP-L system and between samples from the chamber wall and the filter of the ITP-H system, transmission electron microscopy (TEM) observations were performed for samples from the upper wall of the ITP-L system and from the filter in the ITP-H system. The powders randomly collected were placed on carbon-coated Cu TEM grids without dispersant to avoid any reaction between the ultra-fine run products and the dispersant, and then observed with an FE-TEM (JEOL JEM-2100F) equipped with energy dispersive X-ray spectroscopy (EDS).

3. Results

3.1. XRD and TEM Observations

Figure 1 compares the XRD patterns of the collected fine powders. The periclase detected in the XRD pattern of condensates in Run $Al_{80}Si_{10}Mg_{10}$ is an unvaporized residue of the starting material, which reflects the low-energy density of the plasma flame in the ITP-L system. No such residue was observed for the products in Runs $Al_{95}Mg_5$ or $Al_{99}Mg_1$ because of the higher power of the ITP-H system. The XRD patterns of condensates in Runs Si_{100}, Al_7Si_{93}, and $Al_{50}Si_{50}$ show amorphous halos at 15°–30° with no crystalline features indicating that they are amorphous state. Those of $Al_{75}Si_{25}$ and $Al_{90}Si_{10}$ show crystalline peaks in addition to amorphous halos. The other samples (products in Runs Al_{100}, Al_{100}-H, $Al_{99}Mg_5$-H, $Al_{99}Mg_1$-H, and $Al_{80}Si_{10}Mg_{10}$) show sharp peaks of crystals without clear halos due to the amorphous nature of the materials.

The condensed crystalline grains were not indexed as alumina with the hcp packing of oxygen, such as corundum, but instead as aluminas with the fcc oxygen frameworks. The most common alumina based on the fcc packing of oxygen is γ-alumina ($Fd\bar{3}m$) γ-alumina has a defect spinel structure, where Al cations partially occupy four- or six-coordinated interstitial sites of the fcc oxygen sub-lattice. The structural

Table 1
Summary of the Experimental Conditions and Condensates

ITP	Run	Starting Material	$^{*}f_{Al}$	Power (kW)	Frequency (MHz)	Pressure (kPa)	Feeding Rate (mg minute^{-1})	Plasma Discharge Duration (minute)	Carrier Gas Rate (L minute^{-1}) Ar	Sheath Gas Rate (L minute^{-1})		Central Gas Rate (L minute^{-1})		Condensates
										Ar	O_2	Ar	O_2	
ITP-L	Si_{100}	Si	0	6	13.6	40	56	10	3.0	⋯	⋯	30	3	amorphous
	Al_7Si_{93}	Al+Si	0.07	6	13.6	40	80	10	3.0	⋯	⋯	30	3	amorphous
	$Al_{50}Si_{50}$	Al+Si	0.5	6	13.6	40	50	10	3.0	⋯	⋯	30	3	amorphous, mullite
	$Al_{75}Si_{25}$	Al+Si	0.75	6	13.6	40	98	10	3.0	⋯	⋯	30	3	amorphous, mullite
	$Al_{90}Si_{10}$	Al+Si	0.9	6	13.6	40	94	10	3.0	⋯	⋯	30	3	λ-alumina, amorphous
	Al_{100}	Al	1	6	13.6	40	95	10	3.0	⋯	⋯	30	3	δ-alumina
	$Al_{80}Si_{10}Mg_{10}$	Al +MgO+Si	0.8	6	13.6	40	183	10	3.0	⋯	⋯	30	3	γ-alumina, amorphous
ITP-H	$Al_{95}Mg_5$-H	Al+MgO	0.95	30	4	100	170	7	6.5	55	10	5	⋯	γ-alumina, δ-alumina
	$Al_{99}Mg_1$-H	Al+MgO	0.99	30	4	100	200	7	2.5	55	10	5	⋯	δ-alumina
	Al_{100}-H	Al	1	30	4	100	200	7	2.5	55	10	5	⋯	λ-alumina, δ-alumina, unknown phase of alumina (fcc + superlattice)

Note. $^{*}f_{Al} = [Al]/([Al]+[Si]+[Mg])$.

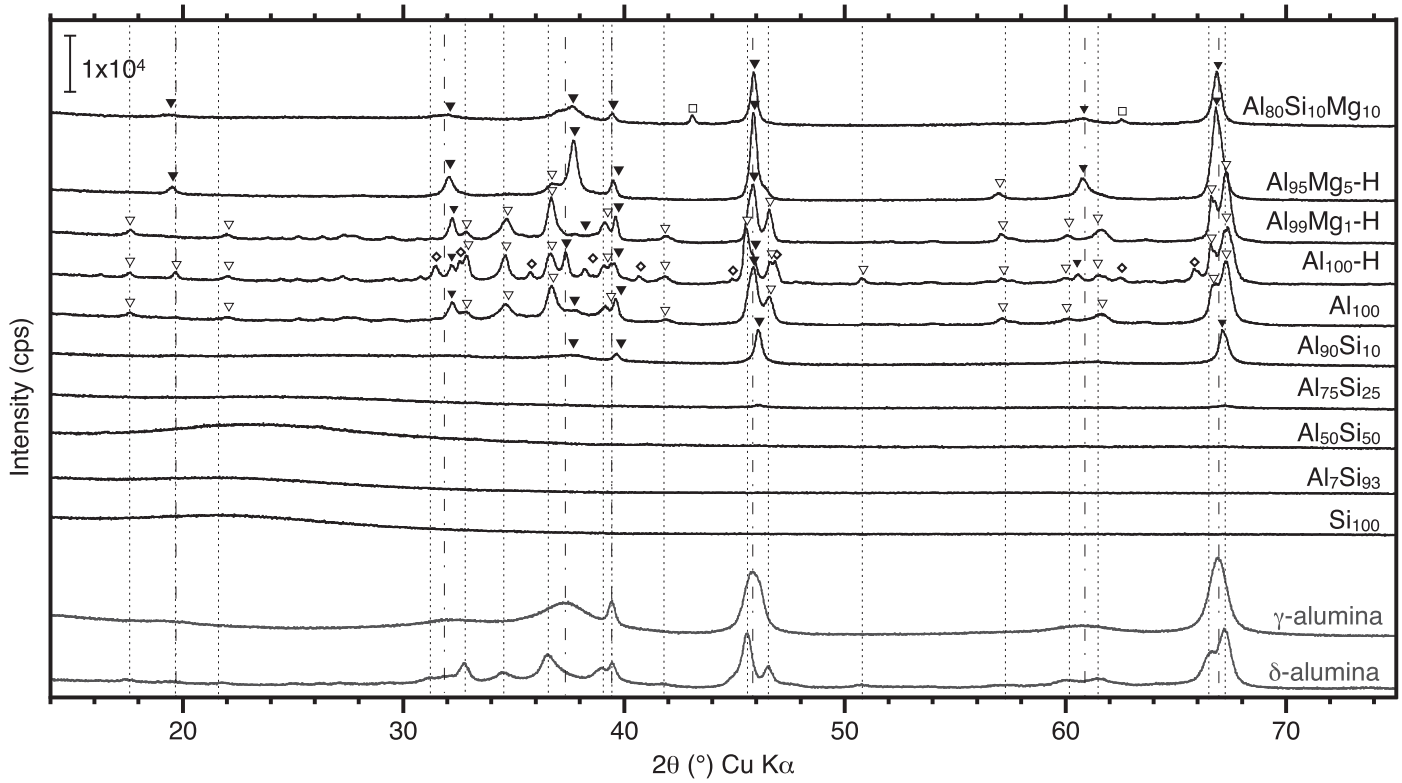

Figure 1. XRD patterns of the condensates and γ- and δ-alumina. Dotted and dashed–dotted lines show the respective peak positions of γ- and δ-alumina. Filled inverted triangles indicate peaks arising from the fcc-packed oxygen. Open inverted triangles indicate δ-alumina. Peaks indicated by open diamonds are attributed to the superlattices of alumina based on the fcc packing of oxygen (unknown phase). Periclase (open rectangle) is a residue of the starting material.

formula of γ-alumina is $(Al_{4/5}V_{1/5})[Al_{28/15}V_{2/15}]O_4$ (Lee et al. 1997), where Al atoms and vacancies (V) in parentheses and brackets represent those in tetrahedral and octahedral sites, respectively. Al atoms and vacancies in both sites are disordered in γ-alumina. The structural differences between γ-, θ-, λ-, and δ-aluminas are based on the differences in the degree of chemical and displacive ordering of Al cations at the interstitial sites of the fcc oxygen subcell (Levin & Brandon 1998; Levin et al. 1998).

The XRD patterns of γ- and δ-aluminas synthesized by sol-gel processing (Takigawa et al. 2014) are also shown in Figure 1. Those of products in Runs $Al_{90}Si_{10}$, $Al_{80}Si_{10}Mg_{10}$, $Al_{95}Mg_5$, and $Al_{75}Si_{25}$ showed that they have structures most similar to γ-alumina, although the peak positions are slightly different. The products in Runs Al_{100}, Al_{100}-H, and $Al_{99}Mg_1$ showed the XRD profiles most similar to δ-alumina ($P2_12_12_1$). The XRD peaks of the condensates in Runs $Al_{99}Mg_1$-H, Al_{100}-H, and Al_{100} at 44°–49° and 62°–72°, where the respective peaks of the 400 and 440 reflections of γ-alumina are expected, are split and their positions are similar to those of δ-alumina. Some additional peaks were also observed for the product in Run Al_{100}-H, as indicated in Figure 1. These additional diffraction peaks do not match any known hcp or fcp alumina phases. The integrated intensities of the XRD peaks of the products in Runs Al_{100}-H, $Al_{99}Mg_1$-H, $Al_{95}Mg_5$-H, Al_{100}, $Al_{90}Si_{10}$, and $Al_{80}Si_{10}Mg_{10}$ at 45°–47°.5, where 400 reflection of γ-alumina appears, were obtained and normalized by that of Al_{100}. The normalized intensities of the products in Runs Al_{100}-H, $Al_{99}Mg_1$-H, and $Al_{95}Mg_5$-H are 0.94–0.97, whereas those of Runs $Al_{90}Si_{10}$, and $Al_{80}Si_{10}Mg_{10}$ were 0.49 and 0.58, respectively. This indicates that about half of the products in Runs $Al_{90}Si_{10}$ and $Al_{80}Si_{10}Mg_{10}$ may be amorphous.

The TEM observations show that the condensed grains in all run products have spherical shapes with the size of <150 nm. The spherical shape of condensates indicates that these grains formed via a transitional liquid state (Ishizuka et al. 2016). Electron diffraction (ED) patterns were taken from >50 nm sized grains. An amorphous halo was only observed in the grains in Run Si_{100} (Figure 2(a)). All grains in Run Al_7Si_{93}, and most grains in Runs $Al_{75}Si_{25}$ and $Al_{50}Si_{50}$, are amorphous as well. Some mullite ($Al_{4+2x}Si_{2-2x}O_{10-x}$, $x = 0.17$–0.59) grains were also observed for the products in Runs $Al_{75}Si_{25}$ and $Al_{50}Si_{50}$, which is consistent with the XRD patterns. The ED patterns confirm that the crystalline grains in Run $Al_{80}Si_{10}Mg_{10}$ have a γ-alumina structure, which has an fcc oxygen framework (Figure 2(b)). Most grains in Run $Al_{95}Mg_5$-H show diffraction patterns of γ-alumina, and some show weak reflections due to superlattices indexed to δ-alumina (Figure 2(c)). Clear ED patterns of δ-alumina were observed for the products in Runs $Al_{99}Mg_1$-H and Al_{100} (Figure 2(d)). The diffraction patterns of the grains in Run Al_{100}-H indicate that they have an fcc oxygen framework with superlattices, but they are different to known transition aluminas based on the fcc packing of oxygen (γ-, θ-, θ'-, θ''-, λ-, δ-, and η-alumina; see Figure 2(e)). The condensed grains in Run $Al_{90}Si_{10}$ contain amorphous and λ-alumina ($P2_1/c$) (Figure 2(f); Levin & Brandon 1998). No pure γ-alumina grains were observed for the product in Run $Al_{90}Si_{10}$, but the intensities of the diffraction spots due to the superlattices are weak compared with those in Runs $Al_{99}Mg_1$-H, Al_{100}-H, and Al_{100} (Figure 2(d)), which is consistent with the XRD pattern

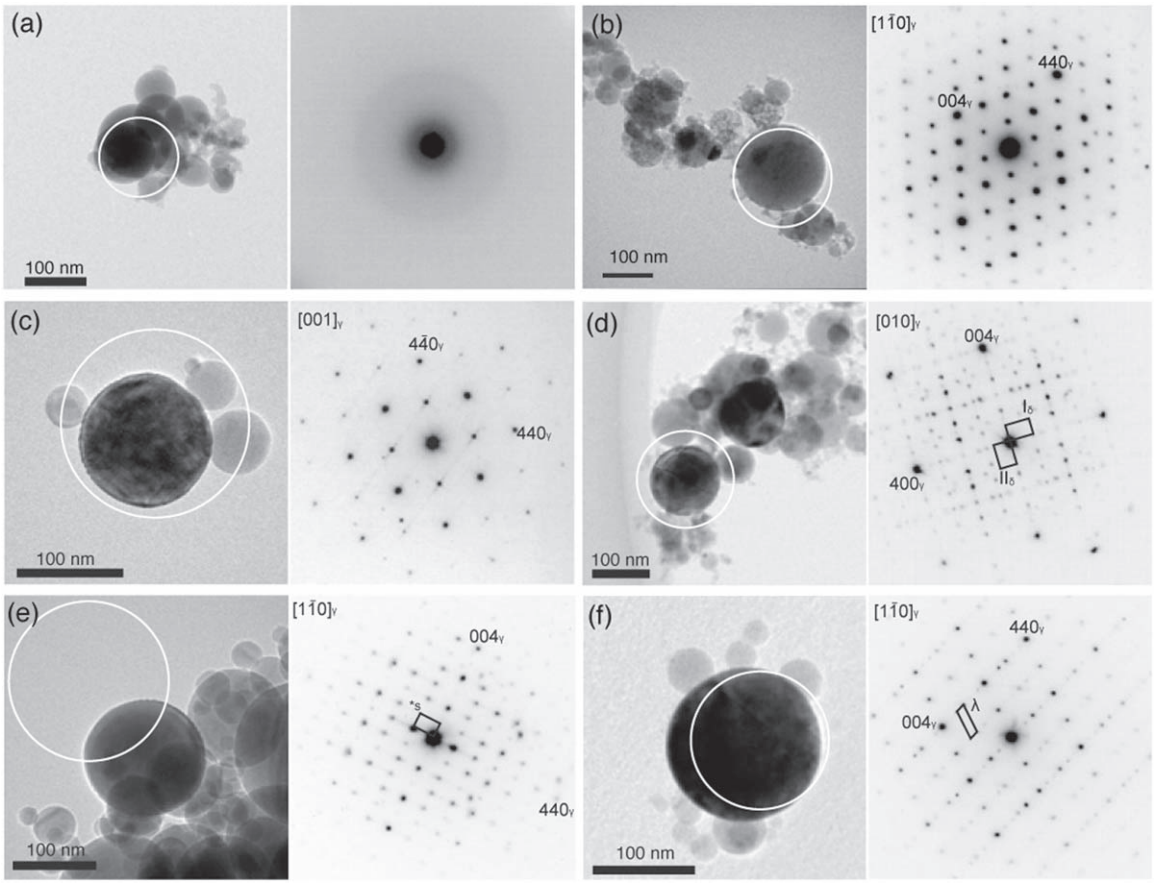

Figure 2. TEM images and ED patterns of products in Runs (a) Si_{100}, (b) $Al_{80}Si_{10}Mg_{10}$, (c) $Al_{95}Mg_5$, (d) Al_{100}, (e) Al_{100}-H, and (f) $Al_{90}Si_{10}$. White circles indicate SAD areas. Superlattice reflections of transition aluminas are indicated in panels (d)–(f).

without split peaks at ∼46° and ∼67° (Figure 1). The principal diffraction spots in Figures 2(b)–(f) are indexed by γ-alumina because they are attributed to reflections by the fcc oxygen sublattices. The phases of the condensates determined by XRD and TEM are summarized in Table 1. EDS mapping was performed for the products in Runs $Al_{90}Si_{10}$, $Al_{75}Si_{25}$, and $Al_{50}Si_{50}$. In the products of Run $Al_{90}Si_{10}$, most of the grains showed almost the same Al contents as the starting material, where the averaged Al content was $f_{Al} = 0.91 \pm 0.03$, and a few small grains (<10 nm in diameter) attached to larger grains (a few tens nm in diameter) are richer in Si than the starting material. The products in Run $Al_{75}Si_{25}$ showed homogeneous chemical composition with the Al content similar to the starting material, but those in Run $Al_{50}Si_{50}$ contains two typed grains: Al-rich and Si-rich. The Al-rich grains ($f_{Al} \sim 0.7$) were relatively larger than the Si-rich grains ($f_{Al} \sim 0.3$). These results indicate that Al and Si were basically incorporated into a single phase with the same ratio as the starting materials if the composition of the starting materials is rich in Al ($f_{Al} > 0.75$).

3.2. FT-IR Spectra

FT-IR spectra of the experimental products are shown in Figure 3. The product in Run Si_{100} shows peaks at 9.1, 12.2, and 21.2 μm, which is consistent with those of amorphous silica. With an increase in Al content, the intensities of the peaks at 9.1 and 21.2 μm decrease and the broad peaks at 11–14 and 15–18 μm become stronger. The peaks at 9.1 and 21.2 μm are attributed to vibrations of the SiO_4 tetrahedra, and the peaks at 11–14 and 15–18 μm are attributed to vibrations of the condensed AlO_4 tetrahedra and AlO_6 octahedra, respectively (Tarte 1967). The FT-IR spectrum of the condensed grains in Run $Al_{80}Si_{10}Mg_{10}$ shows broad double peaks at 12.3 and 13.6 μm. That in Run $Al_{90}Si_{10}$ shows a broad feature with a peak at 12.2 μm and a shoulder at 13.2 μm. Many sharp peaks are observed in addition to the broad feature at ∼12.5–16.0 μm for the spectra of the products in Runs $Al_{95}Mg_5$-H, $Al_{99}Mg_1$-H, Al_{100}-H, and Al_{100}. These sharp peaks reflect the superlattices observed in the ED patterns. The absence of sharp peaks in the FT-IR spectrum of the product in Run $Al_{90}Si_{10}$ indicates a low degree of ordering at the crystallographic sites that form superlattices.

Figure 3 also compares the spectra of the γ- and δ-aluminas synthesized by sol-gel processing (Takigawa et al. 2014), which are the same as those used in the XRD analysis. The spectral profiles of the products in Runs $Al_{80}Si_{10}Mg_{10}$ and $Al_{90}Si_{10}$ are similar to those of the γ-alumina, and the peak profiles of the products in Runs Al_{100}, Al_{100}-H, and $Al_{99}Mg_1$-H, and Run $Al_{95}Mg_5$-H are similar to that of δ-alumina. However, the peaks of these ITP products at 14–20 μm are relatively weaker than the spectra of the γ- and δ-aluminas. This difference comes from the contrasting shapes of the grains. It is well known that spectra are strongly dependent on grain shape (Bohren & Huffman 1983). The condensates in the ITP systems are spheres, whereas the γ- and δ-alumina grains formed by sol-gel processing are rhombic plates (Takigawa et al. 2014). The FT-IR spectral profile of γ-alumina with spherical shapes (Koike et al. 1995) is very

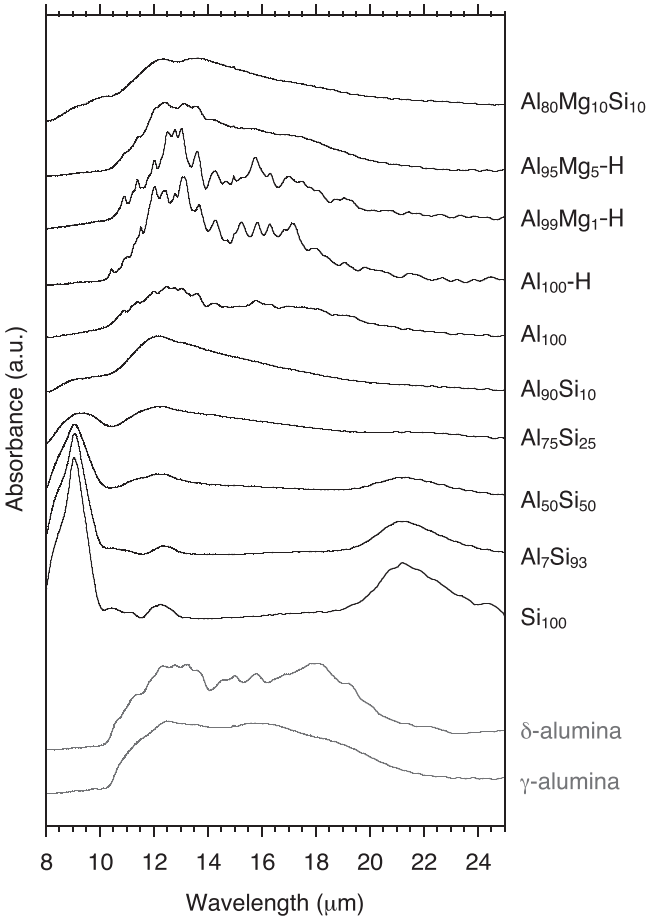

Figure 3. FT-IR spectra of the condensed particles (black) and δ- and γ-aluminas synthesized with sol-gel processing (gray lines; Takigawa et al. 2014).

similar to that of condensates in Run $Al_{90}Si_{10}$ except for the peak width, as shown below.

4. Discussion

4.1. Comparison of the Grain-formation Conditions in ITP Systems and around AGB Stars

Based on nucleation theory, Yamamoto & Hasegawa (1977) introduced dimensionless parameter of Λ to describe grain formation under various conditions. Λ defines the physical conditions of grain formation (Equation (1)).

$$\Lambda = \frac{\nu\tau}{h/k_{\rm B}T_e - 1},\ \nu = \alpha n_0 4\pi a^2 \sqrt{\frac{N_{\rm A}k_{\rm B}T_e}{2\pi m}}. \quad (1)$$

Here, a is radius of vapor molecules, α is sticking probability, n_0 is number density of vapor molecules, $k_{\rm B}$ is the Boltzmann constant, $N_{\rm A}$ is Avogadro constant, $T_{\rm e}$ is equilibrium temperature, h is latent heat of evaporation, and τ is a cooling timescale of the vapor. We estimated Λ of the ITP-H and ITP-L systems to compare the experimental conditions with circumstellar environments. The cooling rate of the ITP-L system was assumed to be similar to that of ITP-H system, and a value of $10^4\,{\rm K\,s^{-1}}$ was adopted (Shigeta & Watanabe 2005), which corresponds to a cooling timescale ($\tau_{\rm T}$) of $\sim$0.1 s. For a rough estimation, we assumed a pure Al-O system and the feeding rates of 200 and 100 mg minute^{-1} as typical values for ITP-H and ITP-L, respectively. The number densities of AlO molecules in the plasmas in the ITP-H and ITP-L systems were estimated from the feeding rates of the starting materials, the flow rates of the Ar and O_2 gases, and the total pressure in the chambers (Table 1). The sticking coefficients ($\alpha_{\rm c}$) of the amorphous and transition alumina are not known, but are probably higher than that of corundum (0.05–0.10; Takigawa et al. 2015). Here we assumed that the $\alpha_{\rm c}$ values of the amorphous and transition aluminas were between 0.1 and 1.0. The estimated Λ values of the ITP-H and ITP-L systems are thus $(0.8–8) \times 10^4$ and $(2–20) \times 10^4$, respectively. The gas density vaporized from the starting material is one of the important factors to determine the diameter of particles. Plasma has temperature and velocity distributions in radial and axial direction (Shigeta & Watanabe 2005), which makes a distribution of gas density vaporized from the starting material. Nucleation and growth of grains at different vapor density and temperature gradient and mixing of those grains result in a broad size distribution of produced particles (Figure 2).

Assuming that the $\tau_{\rm T}$ of the stellar outflow from an AGB star is 4×10^7 s, the total gas pressure is 0.01 Pa, and alumina forms from a gas of solar abundance, Λ is estimated as $(0.1–1) \times 10^4$. The obtained Λ values of the ITP systems and the AGB wind are roughly comparable, indicating that small alumina grains as observed in the experiments may form in circumstellar environments as well. It should be noted that the cooling timescale of dust-formation regions around AGB stars needs to be more carefully discussed because the $\tau_{\rm T}$ of the atmosphere near the star is much slower than the outflow, and complex gas motion due to stellar pulsations should also be considered. Also, this model cannot predict formation of metastable or amorphous grains because $\alpha_{\rm c}$ only represents kinetic barriers for grain growth because diffusion distance of atoms depends on the cooling timescale, and kinetic processes controlling the crystal structures of condensed grains are not taken into account. The transformation of different metastable alumina or corundum via the annealing of amorphous or condensed metastable alumina is another issue that could possibly occur in circumstellar envelopes at low cooling rates.

4.2. Circumstellar Alumina

The FT-IR spectrum of the condensed particles in Run $Al_{90}Si_{10}$ shows a broad feature at $\sim$12 μm without sharp peaks (Figure 3). This should not be directly compared with the circumstellar dust emission because the FT-IR spectra of the samples embedded in KBr pellets are affected by the KBr medium (Tamanai et al. 2009). To compare the observed dust emission with the transmission spectra of the experimental products, we calculated the extinction coefficient ($Q_{\rm ext}$) of the products in Run $Al_{90}Si_{10}$ in a vacuum as a function of wavelength λ (Equation (2)), as follows:

$$\frac{Q_{\rm ext}}{a} = \frac{8\pi}{\lambda}{\rm Im}\left\{\frac{m^2-1}{m^2+1}\right\}, \quad (2)$$

where a is the average radius of the particles and m is the complex refractive index ($m = n + ik$). From the TEM observation, grains are small spherical particles that satisfy $2\pi a/\lambda \ll 1$.

The complex refractive index values of particles embedded in a KBr pellet were deduced by dispersion analysis of the measured

spectrum (Equation (3); Koike et al. 1995; Begemann et al. 1997), as follows:

$$\frac{Q_{\rm ext}}{a} = \frac{2\pi}{\lambda}\left[\frac{24nkn_0^3}{(n^2 - k^2 + 2n_0^2)^2 + 4n^2k^2}\right], \quad (3)$$

where n_0 represents the refractive index of KBr ($n_0 = 1.5$). The result of dispersion analysis is shown in Figure 4(a). The peak position of $Q_{\rm ext}/a$ of the condensates in Run $Al_{90}Si_{10}$ in a vacuum is at 12.0 μm, which is 0.2 μm shorter than that in a KBr pellet. The intensity of the peak at 13 μm relative to that at 12 μm becomes slightly weaker in a vacuum. Figure 4(b) compares the calculated spectra of the product in Run $Al_{90}Si_{10}$ with those of a porous-amorphous alumina by Begemann et al. (1997), and γ-alumina by Eriksson et al. (1981) and Koike et al. (1995). Here, spherical grains much smaller than the wavelength in a vacuum were assumed. The peaks of the product in Run $Al_{90}Si_{10}$ and γ-alumina are at similar wavelengths but at a slightly longer wavelength than for the amorphous alumina. The peak width of the product in Run $Al_{90}Si_{10}$ is between those of the porous-amorphous alumina and γ-alumina. If larger grain sizes are assumed, the peaks will broaden (Min et al. 2006). The spectrum of the grains with continuous distribution of ellipsoids (CDE) show a main peak at 12.1 μm and shallower slope at >12 μm. However, it is unlikely that the CDE-like shape of transition alumina forms via a metastable liquid state.

T Cep is a Mira variable showing a strong "amorphous alumina" feature (SE1t; Sloan et al. 2003). Figure 4(c) compares the dust emission of T Cep and $Q_{\rm ext}/a$ of $Al_{90}Si_{10}$. The *ISO*-SWS spectrum of T Cep at the near-minimum of its period was taken from *ISO* Data archive. A stellar blackbody of 2683 K normalized at 3.0 μm was subtracted from the spectrum of T Cep (Guha Niyogi et al. 2011).

The spectrum of the product in Run $Al_{90}Si_{10}$ in a vacuum is consistent with the broad peak of T Cep at 11–14 μm. The residual spectrum obtained by subtracting $Q_{\rm ext}/a$ of the condensates in Run $Al_{90}Si_{10}$ from T Cep shows peaks at 10.5, 13, and 20 μm (Figure 4(b)). These peaks might relate to emissions from amorphous Mg–Fe silicates or Ca-included aluminosilicate glass (Dorschner et al. 1995; Mutschke et al. 1998), corundum (Zeidler et al. 2013; Takigawa et al. 2015), and FeO (Henning et al. 1995). The present results that (1) amorphous alumina with a pure Al_2O_3 composition does not condense from gases even at very high cooling rates, and (2) the spherical transition aluminas condensed from gases of [Si]/([Al]+[Si]+[Mg]) ~ 0.1 showed the IR spectra with a broad peak at ~12 μm require reinterpretation of dust emission from alumina-rich AGB stars. The transition alumina containing ~10% of Si is the most plausible source of the dust emission from alumina-rich AGB stars.

No presolar transition alumina grain containing Si was reported previously. This is probably because of the sample selection for isotopic measurements. Most of the presolar alumina were identified from acid residues of meteorites (Choi 1998; Nittler et al. 1994, 2008; Stroud et al. 2004; Takigawa et al. 2014, 2018). Corundum is acid resistant but amorphous and transition alumina (κ-, χ-, γ-, θ-, and δ-alumina) are easily dissolved into HF and $HClO_4$ (Takigawa et al. 2014), which are acids commonly used in the acid

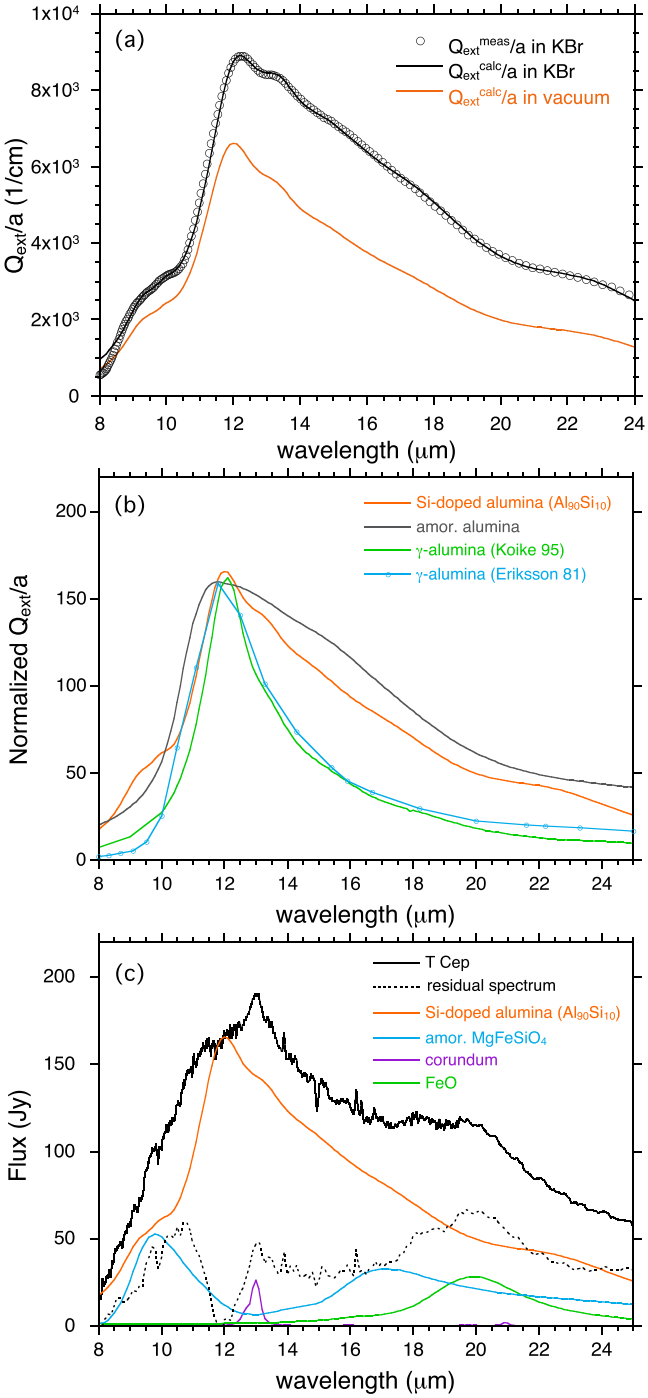

Figure 4. Absorption coefficients of the product in Run $Al_{90}Si_{10}$. Circles indicate the measured FT-IR spectrum of the condensates in Run $Al_{90}Si_{10}$ embedded in the KBr pellet, while the black line shows the fitted result. The orange line shows the calculated spectra of condensates in Run $Al_{90}Si_{10}$ in a vacuum. (b) Comparison of calculated spectra of various aluminas. The orange line is the calculated absorption coefficient of the product in Run $Al_{90}Si_{10}$ in vacuum. The gray line is for spherical porous amorphous alumina (Begemann et al. 1997), and the green and blue lines are spherical γ-alumina from Eriksson et al. (1981) and Koike et al. (1995), respectively. (c) Comparison of the continuum-subtracted spectrum of T Cep (black line) and the calculated absorption coefficient of the product in Run $Al_{90}Si_{10}$ (orange line) in vacuum. The dotted black line indicates the residual spectrum of T Cep subtracted by $Al_{90}Si_{10}$. Also shown are spectra for amorphous $MgFeSiO_4$ (blue line; Dorschner et al. 1995), corundum with a crystal shape that has been slightly flattened to the *c*-axis (purple line; Takigawa et al. 2015), and FeO (green line; Henning et al. 1995).

processing of meteorites. Even if presolar metastable alumina were present in primitive meteorites, they had been lost during acid processing. This also explains the rarity of amorphous presolar alumina. Careful studies both on the chemical composition and crystal structure of individual presolar alumina grains without chemical treatment and prior to the destructive isotopic measurements are needed to conclude the presence of presolar Si-containing transition alumina grains in chondrites.

The authors would like to thank anonymous reviewers for their insightful comments that improved the quality of this Letter. This work was supported by JSPS KAKENHI grant No. 15H05695.

ORCID iDs

Aki Takigawa https://orcid.org/0000-0002-0649-6997
Tae-Hee Kim https://orcid.org/0000-0002-7908-8468
Chiyoe Koike https://orcid.org/0000-0002-9664-7188
Takayuki Watanabe https://orcid.org/0000-0002-0495-1108

References

Begemann, B., Dorschner, J., Henning, T., et al. 1997, ApJ, 476, 199
Bohren, C. F., & Huffman, D. R. 1983, Absorption and Scattering of Light by Small Particles (New York: Wiley)
Cheng, Y., Shigeta, M., Choi, S., & Watanabe, T. 2012, ChEnJ, 183, 483
Choi, B. 1998, Sci, 282, 1284
Chou, T. C., & Nieh, T. G. 1991, JACerS, 74, 2270
Dorschner, J., Begemann, B., Henning, T., Jaeger, C., & Mutschke, H. 1995, A&A, 300, 503
Eriksson, T. S., Hjortsberg, A., Niklasson, G. A., & Granqvist, C. G. 1981, ApOpt, 20, 2742
Guha Niyogi, S., Speck, A. K., & Onaka, T. 2011, ApJ, 733, 93
Gutiérrez, G., & Johansson, B. 2002, PhRvB, 65, 104202
Henning, T., Begemann, B., Mutschke, H., & Dorschner, J. 1995, A&AS, 112, 143
Ishizuka, S., Kimura, Y., Yamazaki, T., et al. 2016, Chemistry of Materials, 28, 8732
Kim, T. H., Tsuchiyama, A., Takigawa, A., & Matsuno, J. 2017, in Int. Symp. Plasma Chemistry P2-33-37 (Montreal: Internal Plasma Chemistry Society), 698
Koike, C., Kaito, C., Yamamoto, T., et al. 1995, Icar, 114, 203
Lee, M.-H., Cheng, C.-F., Heine, V., & Klinowski, J. 1997, CPL, 265, 673
Levin, I., & Brandon, D. 1998, JACerS, 81, 1995
Levin, I., Gemming, T., & Brandon, D. G. 1998, PSSA, 166, 197
Lodders, K. 2003, ApJ, 591, 1220
Maruyama, T., & Arai, S. 1992, ApPhL, 60, 322
Matsuno, J., Tsuchiyama, A., Noda, J., et al. 2014, LPI, 45, 1335
Min, M., Dominik, C., Hovenier, J. W., et al. 2006, A&A, 445, 1005
Mutschke, H., Begemann, B., Dorschner, J., et al. 1998, A&A, 333, 188
Nittler, L., Alexander, C. O. D., Gao, X., Walker, R., & Zinner, E. 1994, Natur, 370, 443
Nittler, L. R., Alexander, C. M. D., Gallino, R., et al. 2008, ApJ, 682, 1450
Ohnaka, K., Weigelt, G., & Hofmann, K. H. 2016, A&A, 597, A20
Ohnaka, K., Weigelt, G., & Hifmann, K.-H. 2017, A&A, 597, A20
Shigeta, M., & Watanabe, T. 2005, JMatR, 20, 2801
Sloan, G. C., Kraemer, K. E., Price, S. D., & Shipman, R. F. 2003, ApJS, 147, 379
Stroud, R. M., Nittler, L. R., & Alexander, C. M. D. 2004, Sci, 305, 1455
Takigawa, A., Kamizuka, T., Tachibana, S., & Yamamura, I. 2017, SciA, 3, eaao2149
Takigawa, A., Stroud, R. M., Nittler, L. R., Alexander, C. M. O. D., & Miyake, A. 2018, ApJL, 862, L13
Takigawa, A., Tachibana, S., Huss, G. R., et al. 2014, GeCoA, 124, 309
Takigawa, A., Tachibana, S., Nagahara, H., & Ozawa, K. 2015, ApJS, 218, 2
Tamanai, A., Mutschke, H., Blum, J., et al. 2009, A&A, 501, 251
Tarte, P. 1967, AcSpA, 23, 2127
Tavakoli, A. H., Maram, P. S., Widgeon, S. J., et al. 2013, The Journal of Physical Chemistry C, 117, 17123
Trunov, M. A., Schoenitz, M., Zhu, X., & Dreizin, E. L. 2005, CoFl, 140, 310
Yakovleva, N., Yakovlev, A., & Chupakhina, E. 2000, TSF, 366, 37
Yamamoto, T., & Hasegawa, H. 1977, PThPh, 58, 816
Zeidler, S., Posch, T., & Mutschke, H. 2013, A&A, 553, A81